Nanoscale Advances

ROYAL SOCIETY OF CHEMISTRY

PAPER

View Article Online
View Journal | View Issue

Cite this: *Nanoscale Adv.*, 2025, **7**, 7171

Electronic and magnetic properties of Janus monolayer Al_2SO modified by defects and doping: a first-principles study

Nguyen Thanh Tien,[a] R. Ponce-Pérez,[b] Armando Reyes-Serrato,[b] J. Guerrero-Sanchez[b] and D. M. Hoat *[cd]

In recent years, two-dimensional (2D) Janus structures have attracted great research attention because of their promise for practical applications. In this work, Janus monolayer Al_2SO under the effects of vacancy and doping is systematically investigated. The pristine Al_2SO monolayer exhibits a direct-gap semiconductor nature with a band gap of 1.52 eV. The chemical bonds Al1–O and Al2–S are predominantly ionic, meanwhile the covalent character dominates the Al1–Al2 bond. A single Al2 vacancy induces a half-metallic nature with a total magnetic moment of 1.00 μ_B, meanwhile no magnetism is obtained by creating a single Al1 vacancy that metallizes the monolayer. The nonmagnetic semiconductor nature is preserved with single O and S vacancies, which tune the band gap to 1.41 and 1.70 eV, respectively. Significant magnetism with an overall magnetic moment of 5.00 μ_B is induced by doping with a single Fe atom. Our simulations assert the antiferromagnetic semiconductor nature of the Fe-doped Al_2SO monolayer, where antiferromagnetism is more stable in the case of pair-Fe-atom substitution with an energy difference of 309.3 meV compared to ferromagnetism. Beyond monoelement doping, the substitution of small clusters of FeN_3 and FeF_3 is also investigated. These clusters induce a feature-rich electronic nature with total magnetic moments of 2.00 and 2.11 μ_B, respectively. In all cases, Fe atoms mainly induce the magnetic moment in the system. Small cluster doping also generates multiple mid-gap energy states around the Fermi level, which is crucial to control the electronic nature of the system. Our study provides new insights into the functionalization of the Janus monolayer Al_2SO that could be employed to make new promising 2D spintronic materials.

Received 10th June 2025
Accepted 29th August 2025

DOI: 10.1039/d5na00569h

rsc.li/nanoscale-advances

I. Introduction

The successful exfoliation of graphene in 2004 [1] marked the starting point for the important field of investigations on two-dimensional (2D) materials. Undoubtedly, graphene is of special interest and it is one of the most investigated 2D materials not only for fundamental research but also for technological applications.[2,3] However, the lack of an intrinsic band gap presents a limitation of graphene that can be overcome by some approaches such as edge cutting[4,5] and surface functionalization.[6,7] Moreover, research efforts have also been made to achieve significant progress in the exploration and discovery of new post-graphene 2D materials, resulting in a large variety of new exciting structures with intriguing physical properties including metallic,[8,9] semiconducting,[10,11] insulating,[12,13] and superconducting properties.[14,15] In this regard, 2D semiconductors are widely explored for the development of diminutive and flexible optoelectronic and electronic devices.[16,17] Among them, 2D materials based on III–VI groups have been successfully prepared in experiments, exhibiting promising optoelectronic performances with high on–off current ratios, high electron mobility, and broad-band spectral response.[18–21] Besides the experimental investigations, great theoretical endeavor has revealed the mechanical flexibility[22,23] and tunable band gap of these materials through thickness engineering[24] and the application of external electric field/strain.[25,26]

Following the great progress of 2D compounds, researchers have paid increasing attention to the development of ternary Janus monolayers. The first theoretical prediction of Janus transition metal dichalcogenides (MXY; M = Mo and W; X, Y = S, Se, and Te) was realized by Cheng *et al.*[27] Later, the first successful fabrication of the Janus structure MoSSe monolayer with intrinsic vertical piezoresponse highlighted significant advancement in the field of 2D materials.[28,29] These achievements have been followed by the successful experimental

[a]*College of Natural Sciences, Can Tho University, 3-2 Road, Can Tho City 900000, Vietnam*

[b]*Universidad Nacional Autónoma de México, Centro de Nanociencias y Nanotecnología, Apartado Postal 14, Ensenada, Baja California, Código Postal 22800, Mexico*

[c]*Institute of Theoretical and Applied Research, Duy Tan University, Ha Noi 100000, Vietnam. E-mail: dominhhoat@duytan.edu.vn*

[d]*School of Engineering and Technology, Duy Tan University, Da Nang 550000, Vietnam*

realization of other Janus structures including WSSe[30] and PtSSe,[31] among others. The formation of Janus structures breaks the out-of-plane symmetry, showing promise for advanced applications in diverse areas such as electronics and optoelectronics,[32,33] piezoelectrics,[34,35] and photocatalysis.[36,37] These experimental achievements have motivated researchers to design a vast array of Janus materials considering the flexible chemical compositions and structures. Particularly, the stability, electronic, optical, piezoelectric, and thermoelectric properties of those based on III-group have been investigated, including Al_2XY, Ga_2XY, and In_2XY.[38–40] Recently, the concept of oxygen-containing Janus structures with oxygen as a third component element has been proposed,[41,42] however deep insights into this material group are still needed since they have not been extensively investigated yet.

On the other hand, chemical modification has been extensively exploited to achieve efficient magnetism engineering in 2D materials in order to add new functionalities. In this regard, substitutional doping may be the most employed route because of its effectiveness and simplicity using transition metals, rare earth metals, and even nonmetals as dopant atoms.[43–47] The investigations are not only limited to monoelement doping, but also doping with multielemental impurities has been considered.[48,49] It has been found that dopant atoms can form small clusters due to strong thermodynamic driving forces. For example, FeN_4 and FeC_4 complexes have been found to be thermodynamically stable in the graphene monolayer.[50,51] Then, several research groups have proposed doping with small clusters in 2D materials for tailoring their electronic properties and magnetic states including FeX_6 and TMO_3 (TM = Mn, Fe, Co, and Ni) in the MoS_2 monolayer,[52,53] TMO_3 and TMO_4 (TM = 3d transition metals) in the BN monolayer,[54] and TMO_n (TM = V, Cr, Mn, and Fe; $n = 3$ and 6) in the PtS_2 monolayer,[55] among others. Results have demonstrated the emergence of feature-rich electronic and magnetic properties induced by cluster doping.

In this work, we investigate systematically the structural stability and electronic properties of the Al_2SO monolayer. The presence of vacancy defects could induce magnetism in this 2D material or effectively tune its electronic structure. Furthermore, we propose doping with the transition metal Fe and small FeZ_3 (Z = N and F) clusters to achieve magnetism engineering of the Al_2SO monolayer in order to add new functionalities.

II. Computational details

Our calculations are based on the density functional theory (DFT),[56] as embedded in Vienna *ab initio* simulation package (VASP) that makes use of the projector augmented wave (PAW) potential to treat ion–electron interactions.[57,58] The generalized gradient approximation (GGA) describes the exchange–correlation functionals, where the PBE version (Perdew–Burke–Ernzerhof) is adopted.[59] The on-site Coulomb interactions of the Fe-3d orbital are properly described by employing the GGA+U method,[60] where an effective Hubbard parameter of 5.40 eV is set in accordance with previous reports.[61,62] A plane-wave cutoff energy of 500 eV is set for the expansion of the valence-electron wave functions (Al: $3s^23p^1$; S: $3s^23p^4$; O: $2s^22p^4$; Fe: $3d^64s^2$; N: $2s^22p^3$; F: $2s^22p^5$). Structures are relaxed until Hellmann–Feynman residual forces on the atoms are smaller than 0.01 eV $Å^{-1}$. The Brillouin zone sampling is realized using a $20 \times 20 \times 1$ k-point grid for the Al_2SO monolayer unit cell, which is generated within the Monkhorst–Pack (MP) scheme.[63] A vacuum gap more than 17 Å is used to eliminate the spurious interactions of the perpendicularly periodic image monolayers.

Phonon dispersion curves of the Al_2SO monolayer are calculated using the density functional perturbation theory (DFPT) implemented in PHONOPY code.[64] In the NVT ensemble, *ab initio* molecular dynamics (AIMD) simulations are carried out using a Nose–Hoover thermostat[65,66] to evaluate the thermal stability of the studied 2D systems at 300 K for 6 ps with a time step of 2 fs (corresponding to 3000 simulation steps).

In order to investigate the impact of vacancy defects and doping, a $4 \times 4 \times 1$ supercell is generated, which contains 64 atoms (32 Al atoms, 16 S atoms, and 16 O atoms). The Brillouin zone of defected/doped systems is integrated using an MP k-point mesh of $4 \times 4 \times 1$. In the case of doping, Fe atoms are doped at Al sublattices due to their metallic nature, while F and N atoms are doped at O sublattices because of their similar atomic size.

III. Results and discussion

A. Stability and electronic properties of the Al_2SO monolayer

Fig. 1a shows the atomic structure of the Al_2SO monolayer in a unit cell that contains one formula unit. It can be seen that two vertically aligned Al atoms are located between O and S atoms. Herein Al atoms linked to O and S atoms are labeled "Al1" and "Al2", respectively. From the structural relaxation, an optimal lattice constant of 3.25 Å is obtained for the Al_2SO monolayer. Moreover, chemical bond lengths d_{Al1-O}, $d_{Al1-Al2}$, and d_{Al2-S} are calculated to be 1.95, 2.61, and 2.24 Å, respectively. The structural parameters of the Al_2SO monolayer are in good agreement with previous reports.[67,68] To check the stability of the Al_2SO monolayer, phonon calculations and AIMD simulations are performed. It is found that there is no nonphysical imaginary mode in the calculated phonon spectra displayed in Fig. 1b, confirming that the Al_2SO monolayer is dynamically stable. During the AIMD simulations, temperature and energy exhibit stable fluctuation in a small range as observed in Fig. 1c. Moreover, the visualized final structure asserts that there is neither significant reconstruction nor a broken bond, preserving the initial configuration. The results confirm that the Al_2SO monolayer is thermally stable.

In order to clarify the electronic properties of the Al_2SO monolayer, we calculated its atom-decomposed band structure and projected density of states. Fig. 2a asserts the Γ–Γ direct-gap semiconductor nature of the Al_2SO monolayer with an energy gap of 1.52 eV. In the considered energy range, O and S atoms make major contributions to the band structure formation, meanwhile Al atoms make little contribution. Specifically, the upper part of the valence band originates primarily from O-$p_{x,y}$ and S-$p_{x,y}$ states, while the Al-s state builds mainly the lower part of the conduction band (see Fig. 2b). To further understand

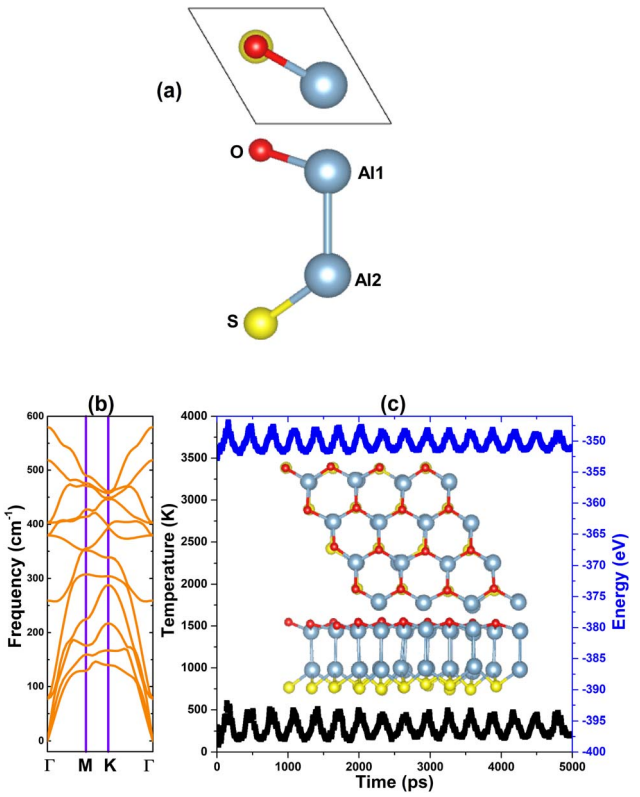

Fig. 1 (a) Atomic structure in a unit cell, (b) phonon dispersion curves, and (c) AIMD simulation at 300 K of the Janus Al_2SO monolayer.

the chemical bonds, the electron localization function (ELF) is visualized in Fig. 2c, which shows the electron enrichment at the O site, S site, and in the Al1–Al2 region. These results suggest that Al atoms transfer charge to O and S atoms because of the difference in their electronegativity. From Bader charge analysis, it is found that the transferred charge quantities from Al1 and Al2 atoms are 1.75 and 1.44 *e*, respectively. Meanwhile, O and S atoms attract charges of 1.69 and 1.50 *e*, respectively. The ELF illustration also demonstrates the covalent character of the Al1–Al2 bond that is generated by the s and p_z hybridization as observed in Fig. 2b.

B. Effects of vacancies

In this part, vacancy (Va_{atom}) effects on the electronic and magnetic properties of the Janus Al_2SO monolayer are investigated (denoted as Va_{atom}@mo). Fig. 3 shows the calculated spin-polarized band structures, where different characteristics are observed depending on the type of vacancy. Specifically, spin-up and spin-down distributions are symmetric upon creating single Va_{Al1}, Va_O, and Va_S vacancies. Note that the upper valence subband of the Va_{Al1}@mo system overlaps with the Fermi level, suggesting the monolayer metallization induced by a single Va_{Al1} vacancy. Meanwhile, the semiconductor nature with band gaps of 1.41 and 1.70 eV are obtained for Va_O@mo and Va_S@mo systems, respectively. These results assert that single Va_O and Va_S vacancies induce band gap reduction of 7.24% and band gap increase of 11.84% in the Al_2SO Janus monolayer, respectively. In contrast, the single vacancy Va_{Al2} induces the asymmetric character of spin-up and spin-down channels, mostly around the Fermi level to confirm the half-metallic nature of the Va_{Al2}@mo system. In this case, an energy gap of 0.72 eV is obtained for the semiconductor spin-up state, meanwhile the spin-down state shows the metallic character.

To get more details on the electronic modification, PDOS spectra of constituent atoms closest to the defect sites are given in Fig. 4. Note that the O-p_z state mainly contributes to the metallic nature of the Va_{Al1}@mo system, where the flat band above the Fermi level is formed mainly from the Al2-p_z state. The single Al1 vacancy leads to the reduced occupancy of O-p

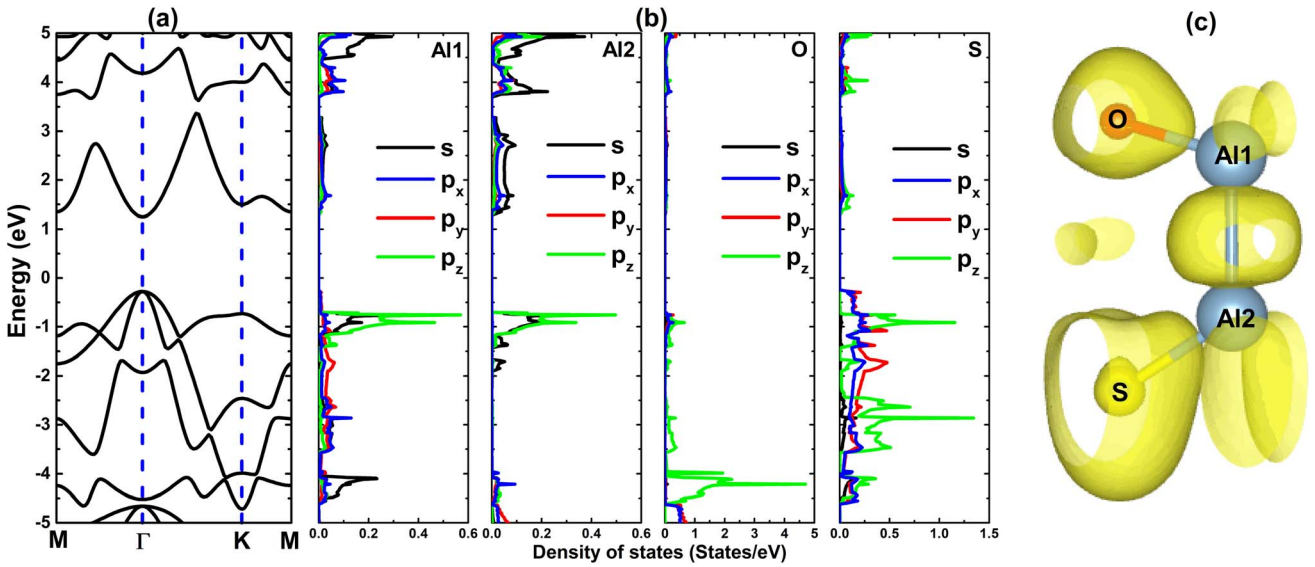

Fig. 2 (a) Electronic band structure, (b) projected density of states (the Fermi level is set to 0 eV), and (c) 3D electron localization function (isosurface value: 0.6 *e* Å^{-3}) of the Janus Al_2SO monolayer.

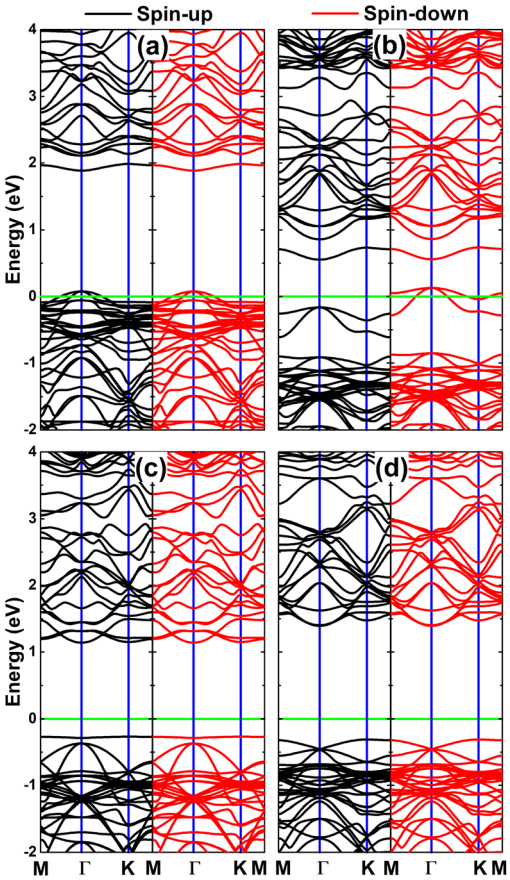

Fig. 3 Spin-polarized band structure of (a) Va_{Al1}@mo, (b) Va_{Al2}@mo, (c) Va_O@mo, and (d) Va_S@mo systems (the Fermi level is set to 0 eV).

orbital, making the valence band shift towards the Fermi level to induce the monolayer metallization. The sub-bands around the Fermi level of the Va_{Al2}@mo system are built primarily from S-$p_{x,y,z}$ states that cause the spin-down metallic character, where the Al1-s state forms the sub-band above the Fermi level in both spin configurations. It is worth mentioning that strong spin polarization in PDOS spectra of the S atom also indicates its key role in generating the magnetism of the system. It is also found that the Al1-p_z state gives rise to a flat band in the upper part of the valence band of the Va_O@mo system, where little contribution from Al1-$p_{x,y}$ is all observed. Similarly, Al2-$p_{x,y,z}$ states also give rise to a new mid-gap sub-band below the Fermi level of the Va_S@mo system, which are mainly responsible for the band gap reduction.

The asymmetric character of spin-up and spin-down bands indicates the magnetic features of the Va_{Al2}@mo system. The overall magnetic moment of the Va_{Al2}-defected system is calculated to be 1.00 μ_B. The spin density illustrated in Fig. 5 demonstrates that the three nearest neighboring S atoms from the defect site contribute mainly to the magnetic moment. Specifically, PDOS spectra in Fig. 4b imply that the S-p orbital contributes primarily to the magnetism of the system, which can be attributed to the absence of a charge losing atom (Al2 vacancy) that causes reduced occupancy of the S-p orbital

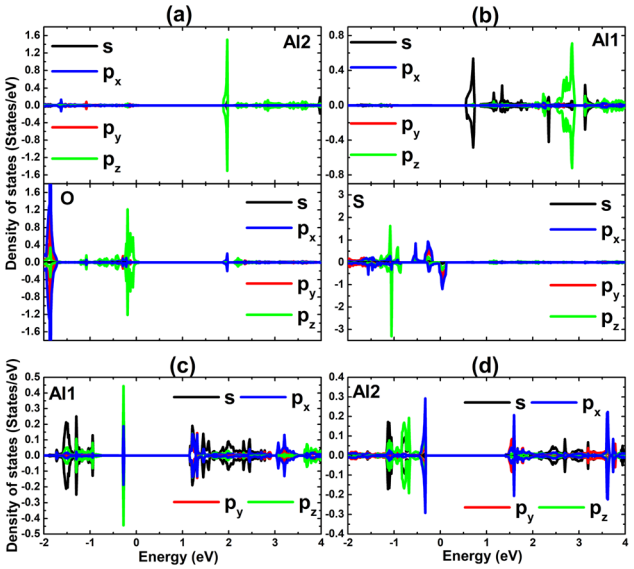

Fig. 4 Spin-polarized projected density of states of constituent atoms closest to the vacancy site in (a) Va_{Al1}@mo, (b) Va_{Al2}@mo, (c) Va_O@mo, and (d) Va_S@mo systems.

around the vacancy site. Consequently, the charge distribution is unbalanced between spin channels to cause spin polarization. Therefore, it can be concluded that the presence of Va_{Al1}, Va_O, and Va_S does not induce magnetism in the Janus Al_2SO monolayer. Meanwhile, significant magnetism with half-metallicity is achieved by creating Va_{Al2} single vacancy. Furthermore, these features are confirmed by computing the difference in energy of the magnetic state (MS) and nonmagnetic state (NMS): $\Delta E = E_{MS} - E_{NSM}$. Positive ΔE values of 0.02, 0.66, and 0.84 eV are obtained for Va_{Al1}@mo, Va_O@mo, and Va_S@mo systems, confirming their nonmagnetic nature since the MS has higher energy than the NMS. In contrast, the MS is found to be

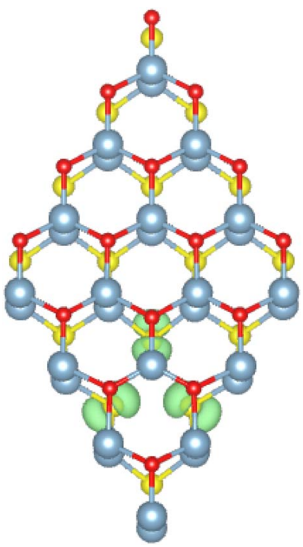

Fig. 5 Spin density (iso-surface value: 0.005 e Å^{-3}) of the Va_{Al2}@mo system.

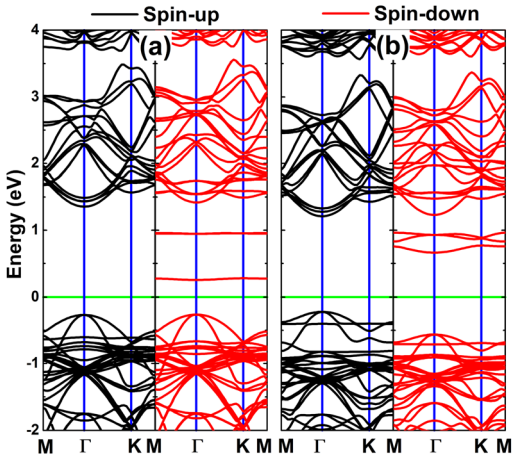

Fig. 6 Spin-polarized band structure of (a) Fe_{Al1}@mo and (b) Fe_{Al2}@mo systems (the Fermi level is set to 0 eV).

energetically more favorable than the NMS for the Va_{Al2}@mo system as confirmed by a negative ΔE value of −0.04 eV.

C. Effects of doping with Fe atom

Herein, doping with Fe atoms is proposed to modify the Al_2SO monolayer's electronic and magnetic properties. Fe_{Al1}@mo and Fe_{Al2}@mo denote the doped systems with Fe doping at Al1 sublattice and Al2 sublattice, respectively. Fig. 6 shows the calculated spin-polarized band structures of Fe_{Al1}@mo and Fe_{Al2}@mo systems. Note that the spin polarization is produced in both cases by the appearance of new mid-gap sub-bands. Importantly, both spin states of Fe-doped Al_2SO monolayers show the semiconductor nature. Specifically, spin-up/spin-down band gaps of 1.62/0.52 and 1.43/1.23 eV are obtained when realizing the Fe substitution at Al1 and Al2 sites, respectively, which are determined mainly by the mid-gap sub-bands.

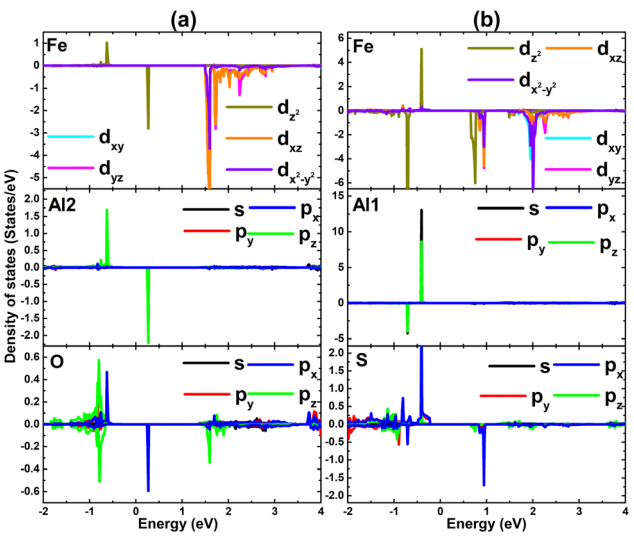

Fig. 7 Spin-polarized projected density of states of Fe impurity and its nearest neighboring atoms in (a) Fe_{Al1}@mo and (b) Fe_{Al2}@mo systems.

To further investigate the origin of these band structure parts, projected density of states (PDOS) spectra of Fe impurity and its nearest neighboring Al and O/S atoms are given in Fig. 7. Note that the flat mid-gap sub-bands are formed primarily from Fe-d_{z^2}–d_{xz}–$d_{x^2-y^2}$, Al-s–p_z, and O/S-$p_{x,y}$ states.

The spin-asymmetric characters suggest the doping-induced magnetization of the Al_2SO monolayer, which is confirmed by the overall magnetic moment of 5.00 μ_B for both Fe_{Al1}@mo and Fe_{Al2}@mo systems. Our simulations also provide local magnetic moments of 3.95 and 3.73 μ_B for Fe impurity in these doped systems, respectively. The spin density in Fe_{Al1}@mo and Fe_{Al2}@mo monolayers is illustrated in Fig. 8a and c, respectively. From the figures, one can see that spin surfaces are produced mainly at Fe atoms. The calculated magnetic moments and illustrated spin density indicate the key role of Fe impurity in generating magnetism in the Janus Al_2SO

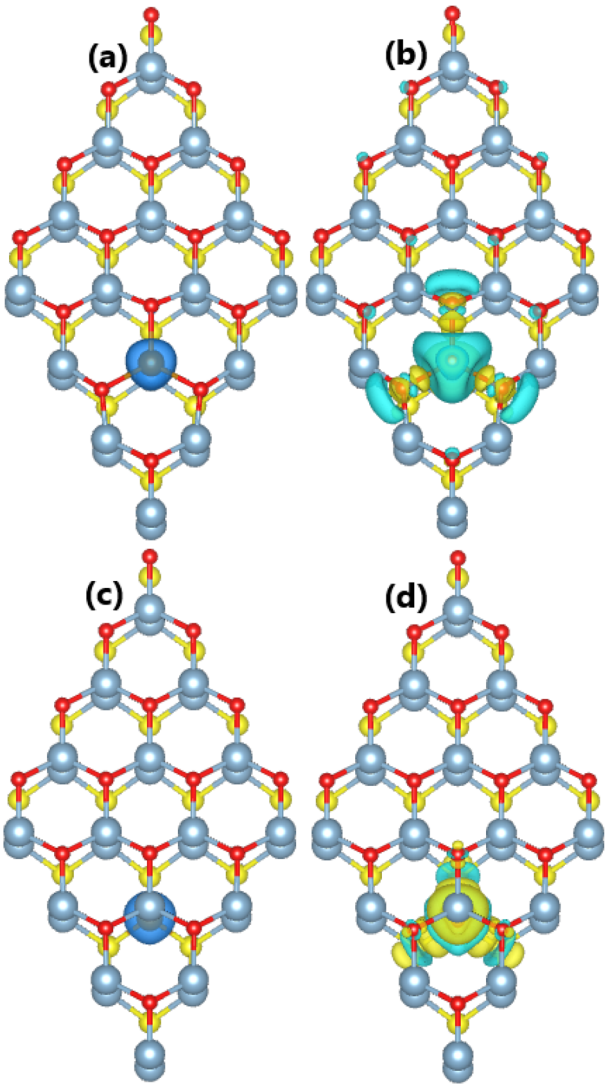

Fig. 8 Spin density (iso-surface value: 0.02 e Å^{-3}) and charge density difference (iso-surface value: 0.003 e Å^{-3}; yellow and aqua surfaces represent the charge accumulation and depletion, respectively) of (a) and (b) Fe_{Al1}@mo and (c) and (d) Fe_{Al2}@mo systems.

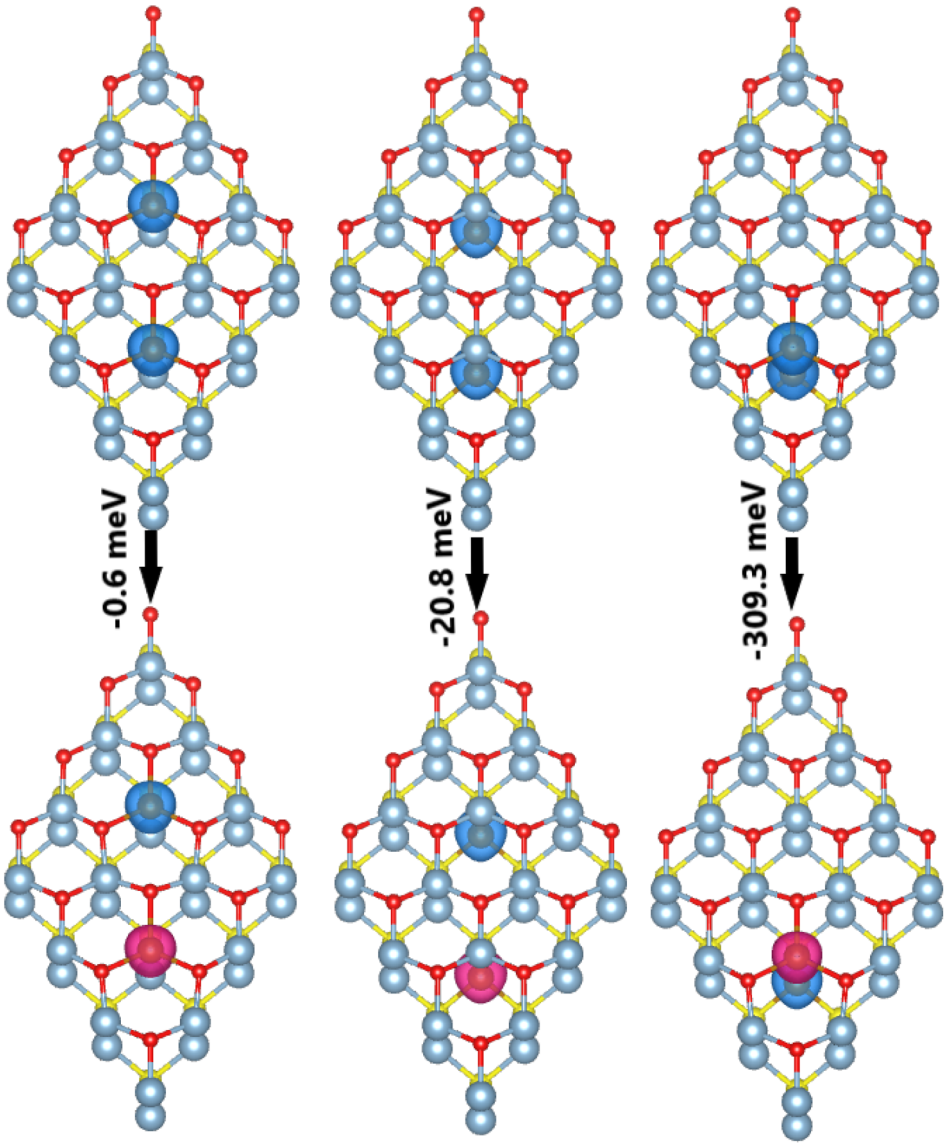

Fig. 9 Energy of the magnetic phase transition of the doped systems: From left to right $2Fe_{Al1}$@mo, $2Fe_{Al2}$@mo, and pFe_{Al12}@mo (iso-surface value: 0.02 e Å^{-3}; blue and pink surfaces represent the positive and negative spin values, respectively).

monolayer. In order to understand the interactions between Fe impurity and the host Al_2SO monolayer, the charge density difference $\Delta\rho$ is calculated as: $\Delta\rho = \rho(\text{ds}) - \rho(\text{mo}) - \rho(\text{Fe})$, where ρ(ds), ρ(mo), and ρ(Fe) denote the charge densities of the doped system, pristine monolayer, and single Fe atom, respectively. Results displayed in Fig. 8b and d assert the charge depletion from Fe atoms and charge enrichment at their nearest neighboring O/S atoms. In addition, the performed Bader charge analysis confirms the transfer of 1.07 and 0.48 e from Fe to the host monolayer in Fe_{Al1}@mo and Fe_{Al2}@mo systems, respectively. Undoubtedly, this difference is derived from the more electronegative nature of O atoms compared to S atom, which leads to higher capability to attract charge from the Fe atom.

In order to study the spin ordering in the Fe-doped Janus Al_2SO monolayer, two-Fe-atom doping approach is applied, where three cases are considered: (1) two Fe atoms are doped at Al1 sites ($2Fe_{Al1}$@mo system); (2) two Fe atoms are doped at Al2 sites ($2Fe_{Al2}$@mo system); and (3) two Fe atoms are doped at two vertically aligned pair of Al atoms (pFe_{Al12} systems). For each system, the total energy of the ferromagnetic (FM) and antiferromagnetic (AFM) states is computed. From Fig. 9, one can see that the AFM state has lower energy than the FM state in all three systems, implying its stability. The difference in energy in $2Fe_{Al1}$@mo, $2Fe_{Al2}$@mo, and pFe_{Al12}@mo systems is calculated to be 0.6, 20.8, and 309.3 meV, respectively. Note that the Fe-atom pair substitution results in highly stable antiferromagnetism in the Janus Al_2SO monolayer.

The spin-polarized band structures of the antiferromagnetic 2Fe-doped Al_2SO monolayers are given in Fig. 10, where one can see the development of new flat mid-gap sub-bands. The antiferromagnetic semiconducting nature is found in $2Fe_{Al1}$@mo, $2Fe_{Al2}$@mo, and pFe_{Al12}@mo systems. Specifically, spin-up/

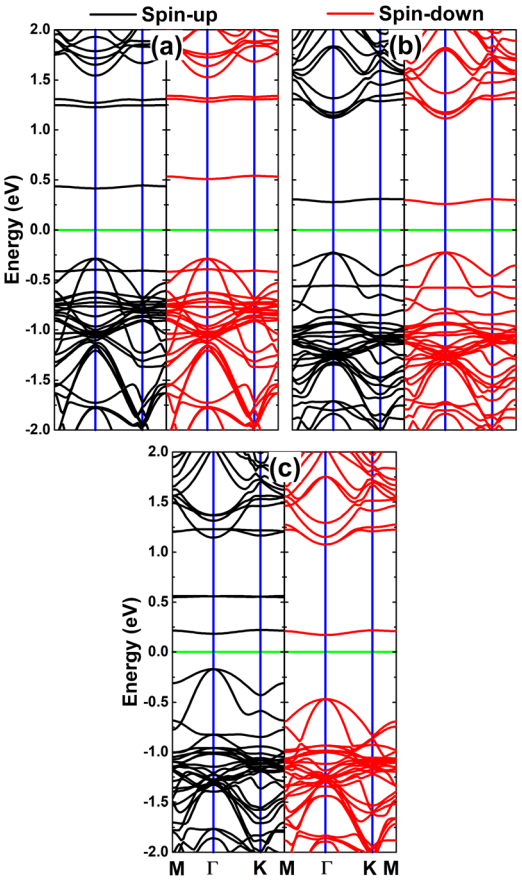

Fig. 10 Spin-polarized band structure of (a) $2Fe_{Al1}$@mo, (b) $2Fe_{Al2}$@mo, and (c) pFe_{Al12}@mo systems (the Fermi level is set to 0 eV).

spin-down energy gaps of 0.70/0.80, 0.50/0.48, and 0.35/0.64 eV are obtained for these systems, respectively. Results suggest the prospective spintronic applications of the antiferromagnetic semiconducting 2Fe-doped Janus Al_2SO monolayers.[69–71]

D. Effects of doping with small FeX_3 (X = N and F) clusters

Beyond monoelement doping, the substitution of small clusters of FeX_3 (X = N and F) in the Janus Al_2SO monolayer is proposed. The doped systems are denoted as FeX_3@mo. The diverse feature-rich electronic nature induced by cluster doping is confirmed by the calculated spin-polarized band structures displayed in Fig. 11. Specifically, the FeN_3@mo system can be classified as a 2D magnetic semiconductor material, whose semiconductor spin-up and spin-down states have energy gaps of 0.22 and 1.58 eV, respectively. Meanwhile, the spin-up state of the FeF_3@mo system exhibits metallic character, giving place to the formation of the half-metallicity. In this case, the semiconductor spin-down state has a band gap of 0.11 eV. Note that the semiconductor nature of the FeN_3@mo system and half-metallic nature of the FeF_3@mo system are regulated by the mid-gap sub-bands, which suggest effective functionalization towards spintronic applications.[72,73] To further investigate their origin, PDOS spectra are given in Fig. 12. Note that the sub-bands around the Fermi level are developed mainly by Fe-d_{z^2}–d_{xz}–$d_{x^2-y^2}$–d_{yz}, N/F-p_y–p_z, and Al-s–p_z states. PDOS profiles also confirm the important role of Fe and N/F atoms of the incorporated small clusters in building the band structure around the Fermi level.

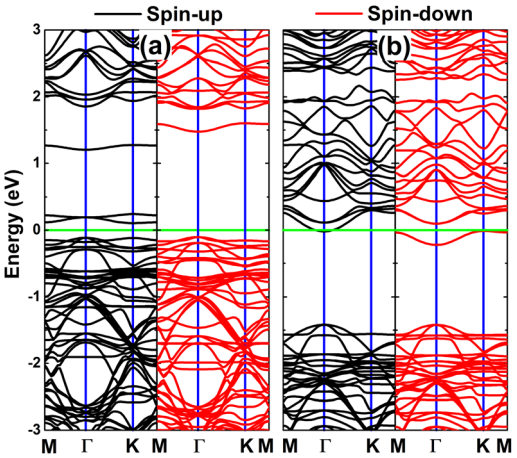

Fig. 11 Spin-polarized band structure of (a) FeN_3@mo and (b) FeF_3@mo systems (the Fermi level is set to 0 eV).

The asymmetry between the spin configurations of FeX_3@mo systems suggests that doping with both small clusters of FeX_3 induces magnetism in the Janus Al_2SO monolayer. Our calculations provide overall magnetic moments of 2.00 and 2.11 μ_B for FeN_3@mo and FeF_3@mo systems, respectively. In these cases, the major contribution comes from Fe atoms with local atomic values of 3.68 and 2.91 μ_B, respectively. These contributions are further visualized by calculating the spin density. From the results given in Fig. 13a and c, one can see spin surfaces centered at Fe sites to confirm their contribution to the system's magnetic moment. From the Bader charge analysis, it is found that the atom in the FeN_3 cluster loses

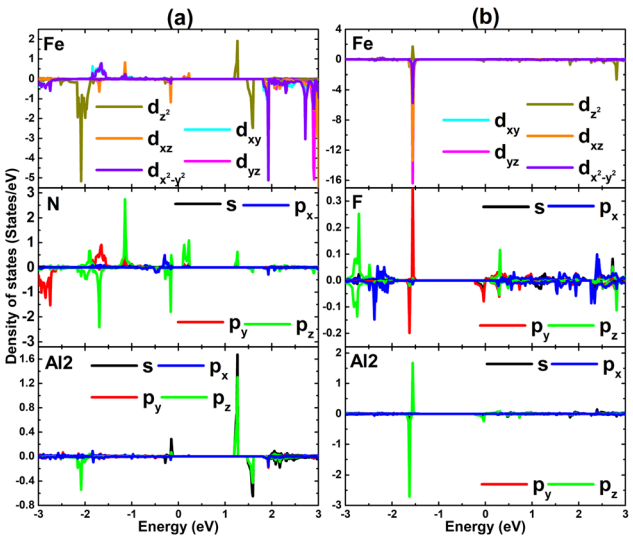

Fig. 12 Spin-polarized projected density of states of Fe impurity and its nearest neighboring atoms in (a) FeN_3@mo and (b) FeF_3@mo systems.

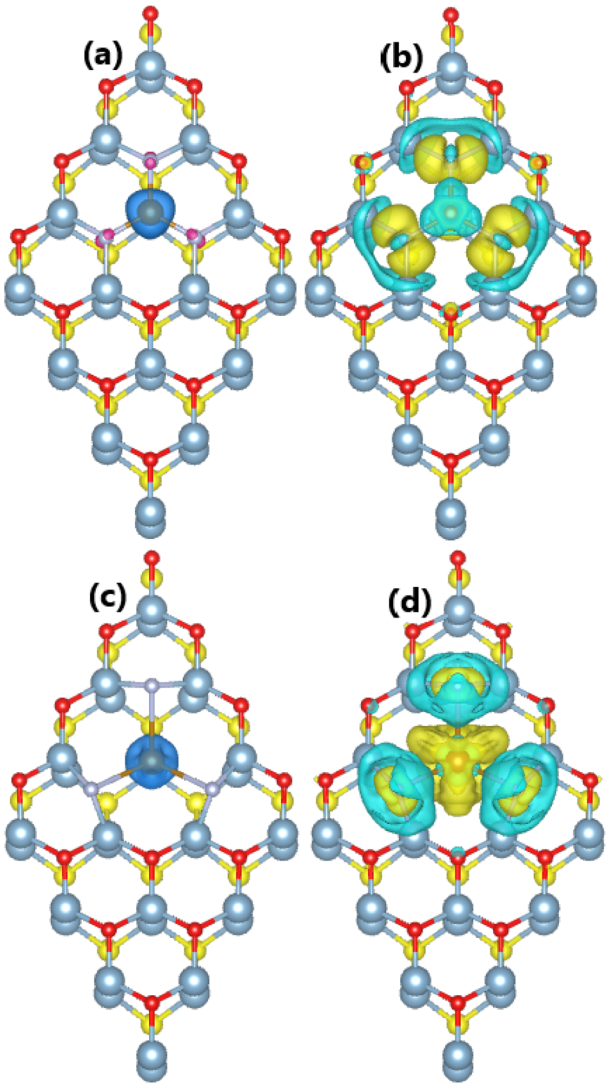

Fig. 13 Spin density (iso-surface value: 0.02 e Å^{-3}) and charge density difference (iso-surface value: 0.003 e Å^{-3}; yellow and aqua surfaces represent the charge accumulation and depletion, respectively) of (a) and (b) FeN_3@mo and (c) and (d) FeF_3@mo systems.

a charge quantity of 0.82 e, meanwhile the Fe atom in the FeF_3 cluster gains 0.29 e. Moreover, each N and F atom attracts charge amounts of 1.84 and 0.96 e, respectively. These electronic interactions are further confirmed by the charge density difference calculated from: $\Delta\rho = \rho(\mathrm{ds}) - \rho(\mathrm{mo}) - \rho(\mathrm{cluster})$. Fig. 13b shows the charge enrichment at N atoms and charge depletion at the Fe atom of the FeN_3 cluster. The charge accumulation is observed at both Fe and F atoms of the FeF_3 cluster (Fig. 13d). These results demonstrate that the small clusters of FeN_3 and FeF_3 attract charges of 4.70 and 3.17 e from the host Al_2SO monolayer, respectively.

E. Formation energy and cohesive energy

Now, the formation energy E_f and cohesive energy E_c of the defected and doped Al_2SO monolayers are calculated using the following formula:

Table 1 Formation energy E_f (eV per atom), cohesive energy E_c (eV per atom), spin-dependent band gap E_f (eV; spin-up/spin-down), charge transfer of impurity ΔQ (e; "+" and "−" represent charge loss and charge gain, respectively), and total magnetic moment M_t (μ_B) of the defected and doped Al_2SO Janus monolayer

	E_f	E_c	E_g	ΔQ	M_t
Va_{Al1}@mo	2.23	−4.86	M/M	—	0.00
Va_{Al2}@mo	3.41	−4.84	0.72/M	—	1.00
Va_O@mo	5.76	−4.80	1.41/1.41	—	0.00
Va_S@mo	1.35	−4.87	1.70/1.70	—	0.00
Fe_{Al1}@mo	0.45	−4.88	1.62/0.52	+1.07	5.00
Fe_{Al2}@mo	1.65	−4.86	1.43/1.23	+0.48	5.00
$2Fe_{Al1}$@mo	0.44	−4.87	0.70/0.80	—	0.00
$2Fe_{Al2}$@mo	1.13	−4.85	0.50/0.48	—	0.00
pFe_{Al12}@mo	0.46	−4.87	0.35/0.64	—	0.00
FeN_3@mo	2.71	−4.80	0.22/1.58	+0.82/−1.84	2.00
FeF_3@mo	0.54	−4.76	M/0.11	−0.29/−0.96	2.11

$$E_f = \frac{E_{ds@mo} - E_{mo} + n_{Al}\mu_{Al} + n_{O/S}\mu_{O/S} - n_{Fe}\mu_{Fe} - n_X\mu_X}{n_{Al} + n_{O/S}} \quad (1)$$

where $E_{ds@mo}$ and E_{mo} are the total energy of the defected/doped and pristine Al_2SO monolayer, respectively; n_{atom} denotes the number of Al/O/S atoms removed and Fe/X atoms incorporated in the system; μ_{atom} refers to the chemical potential of the "atom".

$$E_c = \frac{E_{ds@mo} - m_{Al}E(\mathrm{Al}) - m_O E(\mathrm{O}) - m_S E(\mathrm{S}) - m_{Fe}E(\mathrm{Fe}) - m_X E(\mathrm{X})}{m_{Al} + m_O + m_S + m_{Fe} + m_X} \quad (2)$$

where m_{atom} and E(atoms) represent the number of "atoms" in the system and energy of an isolated "atom", respectively.

The calculated formation energies are listed in Table 1. Note that a single S vacancy is energetically more favorable than a single Al vacancy and single O vacancy because of its smaller formation energy. Our calculations also assert that the Fe atom prefers to replace the Al1 atom since the Fe_{Al1}@mo system has a smaller E_f value than the Fe_{Al2}@mo system. The $2Fe_{Al2}$@mo system may have less thermodynamic favorability than $2Fe_{Al1}$@mo and pFe_{Al12}@mo systems considering its large formation energy. These results suggest that the Fe-atom pair substitution in Al_2SO is a feasible method to realize new 2D antiferromagnetic semiconductor systems with very stable antiferromagnetism. Moreover, the formation of the FeF_3@mo system requires supplying less additional energy than the FeN_3@mo system.

Eqn (2) suggests that structurally and chemically stable systems should have negative E_c values. From Table 1, one can see E_c values between −4.87 and −4.76 eV per atom, indicating good stability of all the defected and doped Al_2SO monolayers.

IV. Conclusions

In summary, first-principles calculations have been performed to investigate systematically the electronic and magnetic properties of the Janus monolayer Al_2SO under the effects of vacancy

defects and doping. This 2D Janus structure has good dynamic and thermal stability. Its nonmagnetic semiconductor nature has also been confirmed; the band structure is formed from Al-s, Al-p, O-p, and S-p orbitals. Moreover, the mix of covalent and ionic chemical bonds is confirmed from the electron localization function. The single Al1 vacancy metallizes the monolayer, meanwhile O and S single vacancies preserve its semiconductor characteristic. The half-metallicity is obtained from the single Al2 vacancy, where magnetic moment is produced primarily by S atoms closest to the Al2 vacancy site. The single Fe impurity generates a total magnetic moment of 5.00 μ_B in the Al_2SO monolayer which is derived mainly from Fe-3d electrons, for which the magnetic semiconductor characteristic is obtained. The energetic stability of the AFM state over the FM state has been found considering the difference in energy of 0.60, 20.80, and −309.30 meV for $2Fe_{Al1}$@mo, $2Fe_{Al2}$@mo, and pFe_{Al12}@mo systems, respectively. Along with the calculated spin-polarized band structure, the antiferromagnetic semiconductor nature is confirmed for these systems. The substitution of small clusters is also predicted to be effective for the magnetism engineering. Specifically, the FeN_3 cluster gives rise to the magnetic semiconductor nature with a total magnetic moment of 2.00 μ_B, while the half-metallicity is obtained from the FeF_3 cluster with an overall magnetic moment of 2.11 μ_B. Bader charge analysis asserts the charge gain of these small clusters that attract charge quantities of 4.70 and 3.17 *e* from the host Al_2SO monolayer, respectively. Our findings may provide good theoretical guidance to make new promising 2D spintronic materials from a nonmagnetic Janus Al_2SO monolayer.

Conflicts of interest

The authors declare that they have no known competing financial interests or personal relationships that could have appeared to influence the work reported in this paper.

Data availability

Data will be provided on request to the authors.

Acknowledgements

Calculations were performed at the DGCTIC-UNAM Supercomputing Center (projects LANCAD-UNAM-DGTIC-368).

References

1 K. S. Novoselov, A. K. Geim, S. V. Morozov, D.-e. Jiang, Y. Zhang, S. V. Dubonos, I. V. Grigorieva and A. A. Firsov, Electric field effect in atomically thin carbon films, *science*, 2004, **306**(5696), 666–669.

2 D. R. Cooper, B. D'Anjou, N. Ghattamaneni, B. Harack, M. Hilke, A. Horth, N. Majlis, M. Massicotte, L. Vandsburger, E. Whiteway, *et al.*, Experimental review of graphene, *Int. Scholarly Res. Not.*, 2012, **2012**(1), 501686.

3 W. Choi, I. Lahiri, R. Seelaboyina and Y. S. Kang, Synthesis of graphene and its applications: a review, *Crit. Rev. Solid State Mater. Sci.*, 2010, **35**(1), 52–71.

4 M. Y. Han, B. Özyilmaz, Y. Zhang and P. Kim, Energy band-gap engineering of graphene nanoribbons, *Phys. Rev. Lett.*, 2007, **98**(20), 206805.

5 Y.-W. Son, M. L. Cohen and S. G. Louie, Energy gaps in graphene nanoribbons, *Phys. Rev. Lett.*, 2006, **97**(21), 216803.

6 B. Guo, L. Fang, B. Zhang and J. R. Gong, Graphene doping: a review, *Insci. J.*, 2011, **1**(2), 80–89.

7 T. Kuila, S. Bose, A. K. Mishra, P. Khanra, N. H. Kim and J. H. Lee, Chemical functionalization of graphene and its applications, *Prog. Mater. Sci.*, 2012, **57**(7), 1061–1105.

8 B. Zhao, D. Shen, Z. Zhang, P. Lu, M. Hossain, J. Li, B. Li and X. Duan, 2D metallic transition-metal dichalcogenides: structures, synthesis, properties, and applications, *Adv. Funct. Mater.*, 2021, **31**(48), 2105132.

9 X. Wan, E. Chen, J. Yao, M. Gao, X. Miao, S. Wang, Y. Gu, S. Xiao, R. Zhan, K. Chen, *et al.*, Synthesis and characterization of metallic Janus MoSH monolayer, *ACS Nano*, 2021, **15**(12), 20319–20331.

10 T. Daeneke, P. Atkin, R. Orrell-Trigg, A. Zavabeti, T. Ahmed, S. Walia, M. Liu, Y. Tachibana, M. Javaid, A. D. Greentree, *et al.*, Wafer-scale synthesis of semiconducting SnO monolayers from interfacial oxide layers of metallic liquid tin, *ACS Nano*, 2017, **11**(11), 10974–10983.

11 C. Cong, J. Shang, X. Wu, B. Cao, N. Peimyoo, C. Qiu, L. Sun and T. Yu, Synthesis and optical properties of large-area single-crystalline 2D semiconductor WS_2 monolayer from chemical vapor deposition, *Adv. Opt. Mater.*, 2014, **2**(2), 131–136.

12 H. Zhang, M. Holbrook, F. Cheng, H. Nam, M. Liu, C.-R. Pan, D. West, S. Zhang, M.-Y. Chou and C.-K. Shih, Epitaxial growth of two-dimensional insulator monolayer honeycomb BeO, *ACS Nano*, 2021, **15**(2), 2497–2505.

13 K. K. Kim, A. Hsu, X. Jia, S. M. Kim, Y. Shi, M. Hofmann, D. Nezich, J. F. Rodriguez-Nieva, M. Dresselhaus, T. Palacios, *et al.*, Synthesis of monolayer hexagonal boron nitride on Cu foil using chemical vapor deposition, *Nano Lett.*, 2012, **12**(1), 161–166.

14 H. Wang, X. Huang, J. Lin, J. Cui, Y. Chen, C. Zhu, F. Liu, Q. Zeng, J. Zhou, P. Yu, *et al.*, High-quality monolayer superconductor $NbSe_2$ grown by chemical vapour deposition, *Nat. Commun.*, 2017, **8**(1), 394.

15 J. Li, P. Song, J. Zhao, K. Vaklinova, X. Zhao, Z. Li, Z. Qiu, Z. Wang, L. Lin, M. Zhao, *et al.*, Printable two-dimensional superconducting monolayers, *Nat. Mater.*, 2021, **20**(2), 181–187.

16 S. Kang, D. Lee, J. Kim, A. Capasso, H. S. Kang, J.-W. Park, C.-H. Lee and G.-H. Lee, 2D semiconducting materials for electronic and optoelectronic applications: potential and challenge, *2D Materials*, 2020, **7**(2), 022003.

17 F. Wang, Z. Wang, C. Jiang, L. Yin, R. Cheng, X. Zhan, K. Xu, F. Wang, Y. Zhang and J. He, Progress on electronic and optoelectronic devices of 2D layered semiconducting materials, *Small*, 2017, **13**(35), 1604298.

18 X. Wang, Y. Sheng, R.-J. Chang, J. K. Lee, Y. Zhou, S. Li, T. Chen, H. Huang, B. F. Porter, H. Bhaskaran, *et al.*, Chemical vapor deposition growth of two-dimensional monolayer gallium sulfide crystals using hydrogen reduction of Ga_2S_3, *ACS Omega*, 2018, **3**(7), 7897–7903.

19 P. Hu, Z. Wen, L. Wang, P. Tan and K. Xiao, Synthesis of few-layer GaSe nanosheets for high performance photodetectors, *ACS Nano*, 2012, **6**(7), 5988–5994.

20 T. Afaneh, A. Fryer, Y. Xin, R. H. Hyde, N. Kapuruge and H. R. Gutierrez, Large-area growth and stability of monolayer gallium monochalcogenides for optoelectronic devices, *ACS Appl. Nano Mater.*, 2020, **3**(8), 7879–7887.

21 H.-C. Chang, C.-L. Tu, K.-I. Lin, J. Pu, T. Takenobu, C.-N. Hsiao and C.-H. Chen, Synthesis of large-area InSe monolayers by chemical vapor deposition, *Small*, 2018, **14**(39), 1802351.

22 M. Yagmurcukardes, R. T. Senger, F. M. Peeters and H. Sahin, Mechanical properties of monolayer GaS and GaSe crystals, *Phys. Rev. B*, 2016, **94**(24), 245407.

23 Y. Li, C. Yu, Y. Gan, Y. Kong, P. Jiang, D.-F. Zou, P. Li, X.-F. Yu, R. Wu, H. Zhao, *et al.*, Elastic properties and intrinsic strength of two-dimensional InSe flakes, *Nanotechnology*, 2019, **30**(33), 335703.

24 Y. Ma, Y. Dai, M. Guo, L. Yu and B. Huang, Tunable electronic and dielectric behavior of GaS and GaSe monolayers, *Phys. Chem. Chem. Phys.*, 2013, **15**(19), 7098–7105.

25 H. Jin, J. Li, Y. Dai and Y. Wei, Engineering the electronic and optoelectronic properties of InX (X = S, Se, Te) monolayers via strain, *Phys. Chem. Chem. Phys.*, 2017, **19**(6), 4855–4860.

26 D. Q. Khoa, D. T. Nguyen, C. V. Nguyen, V. T. Vi, H. V. Phuc, L. T. Phuong, B. D. Hoi and N. N. Hieu, Modulation of electronic properties of monolayer InSe through strain and external electric field, *Chem. Phys.*, 2019, **516**, 213–217.

27 Y. Cheng, Z. Zhu, M. Tahir and U. Schwingenschlögl, Spin–orbit-induced spin splittings in polar transition metal dichalcogenide monolayers, *Europhys. Lett.*, 2013, **102**(5), 57001.

28 A.-Y. Lu, H. Zhu, J. Xiao, C.-P. Chuu, Y. Han, M.-H. Chiu, C.-C. Cheng, C.-W. Yang, K.-H. Wei, Y. Yang, *et al.*, Janus monolayers of transition metal dichalcogenides, *Nat. Nanotechnol.*, 2017, **12**(8), 744–749.

29 J. Zhang, S. Jia, I. Kholmanov, L. Dong, D. Er, W. Chen, H. Guo, Z. Jin, V. B. Shenoy, L. Shi, *et al.*, Janus monolayer transition-metal dichalcogenides, *ACS Nano*, 2017, **11**(8), 8192–8198.

30 S. B. Harris, Y.-C. Lin, A. A. Puretzky, L. Liang, O. Dyck, T. Berlijn, G. Eres, C. M. Rouleau, K. Xiao and D. B. Geohegan, Real-time diagnostics of 2D crystal transformations by pulsed laser deposition: controlled synthesis of Janus WSSe monolayers and alloys, *ACS Nano*, 2023, **17**(3), 2472–2486.

31 R. Sant, M. Gay, A. Marty, S. Lisi, R. Harrabi, C. Vergnaud, M. T. Dau, X. Weng, J. Coraux, N. Gauthier, *et al.*, Synthesis of epitaxial monolayer Janus SPtSe, *npj 2D Mater. Appl.*, 2020, **4**(1), 41.

32 W. Ahmad, Y. Wang, J. Kazmi, U. Younis, N. M. Mubarak, S. H. Aleithan, A. I. Channa, W. Lei and Z. Wang, Janus 2D transition metal dichalcogenides: research progress, optical mechanism and future prospects for optoelectronic devices, *Laser Photonics Rev.*, 2025, **19**(6), 2400341.

33 L. Zhang, Z. Yang, T. Gong, R. Pan, H. Wang, Z. Guo, H. Zhang and X. Fu, Recent advances in emerging Janus two-dimensional materials: from fundamental physics to device applications, *J. Mater. Chem. A*, 2020, **8**(18), 8813–8830.

34 L. Dong, J. Lou and V. B. Shenoy, Large in-plane and vertical piezoelectricity in Janus transition metal dichalcogenides, *ACS Nano*, 2017, **11**(8), 8242–8248.

35 A. Rawat, M. K. Mohanta, N. Jena, Dimple, R. Ahammed and A. De Sarkar, Nanoscale interfaces of Janus monolayers of transition metal dichalcogenides for 2D photovoltaic and piezoelectric applications, *J. Phys. Chem. C*, 2020, **124**(19), 10385–10397.

36 Z. Li, J. Hou, B. Zhang, S. Cao, Y. Wu, Z. Gao, X. Nie and L. Sun, Two-dimensional Janus heterostructures for superior Z-scheme photocatalytic water splitting, *Nano Energy*, 2019, **59**, 537–544.

37 A. Huang, W. Shi and Z. Wang, Optical properties and photocatalytic applications of two-dimensional Janus group-III monochalcogenides, *J. Phys. Chem. C*, 2019, **123**(18), 11388–11396.

38 Y. Zhao, Q. Tan, H. Li, Z. Li, Y. Wang and L. Ma, Tunable electronic and photoelectric properties of Janus group-III chalcogenide monolayers and based heterostructures, *Sci. Rep.*, 2024, **14**(1), 10698.

39 S. Yao, X. Ma, C. Huang, Y. Guo, Y. Ren and N. Ma, Tuning the electronic and piezoelectric properties of Janus Ga_2XY (X/Y = S, Se, Te) monolayers: a first-principles calculation, *Mater. Sci. Semicond. Process.*, 2024, **178**, 108367.

40 D. Xu, B. Cai, J. Tan and G. Ouyang, Tailoring the anisotropic effect of Janus In_2XY (X/Y = S, Se, Te) monolayers toward realizing multifunctional optoelectronic device applications, *New J. Phys.*, 2023, **25**(8), 083013.

41 D. K. Nguyen, J. Guerrero-Sanchez and D. Hoat, HfXO (X = S and Se) Janus monolayers as promising two-dimensional platforms for optoelectronic and spintronic applications, *J. Mater. Res.*, 2023, **38**(9), 2600–2612.

42 M. Demirtas and B. Ozdemir, Oxygenation of monolayer gallium monochalcogenides: design of two-dimensional ternary Ga_2XO structures (X = S, Se, Te), *Phys. Rev. B*, 2020, **101**(7), 075423.

43 L. Chhana, R. C. Tiwari, B. Chettri, D. Rai, S. Gurung and L. Zuala, Ab initio investigation of non-metal-doped ZnS monolayer, *Appl. Phys. A: Mater. Sci. Process.*, 2021, **127**(9), 729.

44 L. Chhana, L. Vanchhawng, D. P. Rai, R. C. Tiwari and L. Zuala, Comparative study of half-metallic ferromagnetic behaviour in ZnO monolayer doped with boron and carbon atoms, *Int. Nano Lett.*, 2021, **11**(2), 113–123.

45 A. Es-Smairi, N. Fazouan, E. Maskar, I. Bziz, M. Sabil, A. Banik and D. Rai, Rare earth (Tm, Y, Gd, and Eu) doped

ZnS monolayer: a comparative first-principles study, *Electron. Struct.*, 2024, **6**(1), 015001.
46 X.-L. Fan, Y.-R. An and W.-J. Guo, Ferromagnetism in transitional metal-doped MoS_2 monolayer, *Nanoscale Res. Lett.*, 2016, **11**(1), 154.
47 D. Shen, B. Zhao, Z. Zhang, H. Zhang, X. Yang, Z. Huang, B. Li, R. Song, Y. Jin, R. Wu, *et al.*, Synthesis of group VIII magnetic transition-metal-doped monolayer $MoSe_2$, *ACS Nano*, 2022, **16**(7), 10623–10631.
48 P. A. Denis, C. Pereyra Huelmo and A. Martins, Band gap opening in dual-doped monolayer graphene, *J. Phys. Chem. C*, 2016, **120**(13), 7103–7112.
49 X. Zhao, R. Huang, T. Wang, X. Dai, S. Wei and Y. Ma, Steady semiconducting properties of monolayer $PtSe_2$ with non-metal atom and transition metal atom doping, *Phys. Chem. Chem. Phys.*, 2020, **22**(10), 5765–5773.
50 A. T. Lee, J. Kang, S.-H. Wei, K.-J. Chang and Y.-H. Kim, Carrier-mediated long-range ferromagnetism in electron-doped Fe-C_4 and Fe-N_4 incorporated graphene, *Phys. Rev. B: Condens. Matter Mater. Phys.*, 2012, **86**(16), 165403.
51 W. I. Choi, S.-H. Jhi, K. Kim and Y.-H. Kim, Divacancy-nitrogen-assisted transition metal dispersion and hydrogen adsorption in defective graphene: a first-principles study, *Phys. Rev. B: Condens. Matter Mater. Phys.*, 2010, **81**(8), 085441.
52 N. Feng, W. Mi, Y. Cheng, Z. Guo, U. Schwingenschlögl and H. Bai, First principles prediction of the magnetic properties of Fe-X_6 (X = S, C, N, O, F) doped monolayer MoS_2, *Sci. Rep.*, 2014, **4**(1), 3987.
53 D. Li, Y. Niu, H. Zhao, C. Liang and Z. He, Electronic and magnetic properties of 3D-metal trioxides superhalogen cluster-doped monolayer MoS_2: a first-principles study, *Phys. Lett. A*, 2014, **378**(22–23), 1651–1656.
54 J. Meng, D. Li, Y. Niu, H. Zhao, C. Liang and Z. He, Structural, electronic, and magnetic properties of 3D metal trioxide and tetraoxide superhalogen cluster-doped monolayer BN, *Phys. Lett. A*, 2016, **380**(29–30), 2300–2306.
55 N. T. Tien, J. Guerrero-Sanchez and D. Hoat, A systematic study of TMO_n (TM = V, Cr, Mn, and Fe; n = 3 and 6) clusters embedded in a PtS_2 monolayer, *Nanoscale Adv.*, 2024, **6**(22), 5671–5680.
56 W. Kohn and L. J. Sham, Self-consistent equations including exchange and correlation effects, *Phys. Rev. A*, 1965, **140**(4), A1133, DOI: **10.1103/PhysRev.140.A1133**.
57 G. Kresse and J. Furthmüller, Efficiency of ab-initio total energy calculations for metals and semiconductors using a plane-wave basis set, *Comput. Mater. Sci.*, 1996, **6**(1), 15–50, DOI: **10.1016/0927-0256(96)00008-0**.
58 G. Kresse and J. Furthmüller, Efficient iterative schemes for ab initio total-energy calculations using a plane-wave basis set, *Phys. Rev. B: Condens. Matter Mater. Phys.*, 1996, **54**(16), 11169, DOI: **10.1103/PhysRevB.54.11169**.
59 J. P. Perdew, K. Burke and M. Ernzerhof, Generalized gradient approximation made simple, *Phys. Rev. Lett.*, 1996, **77**(18), 3865, DOI: **10.1103/PhysRevLett.77.3865**.
60 S. L. Dudarev, G. A. Botton, S. Y. Savrasov, C. Humphreys and A. P. Sutton, Electron-energy-loss spectra and the structural stability of nickel oxide: an LSDA+U study, *Phys. Rev. B: Condens. Matter Mater. Phys.*, 1998, **57**(3), 1505, DOI: **10.1103/PhysRevB.57.1505**.
61 Y. Wang, S. Li and J. Yi, Transition metal-doped tin monoxide monolayer: a first-principles study, *J. Phys. Chem. C*, 2018, **122**(8), 4651–4661, DOI: **10.1021/acs.jpcc.7b12282**.
62 T. V. Vu, V. H. Chu, J. Guerrero-Sanchez and D. Hoat, Regulating the electronic and magnetic properties of a SnSSe Janus monolayer toward optoelectronic and spintronic applications, *ACS Appl. Electron. Mater.*, 2024, **6**(5), 3647–3656.
63 H. J. Monkhorst and J. D. Pack, Special points for Brillouin-zone integrations, *Phys. Rev. B*, 1976, **13**(12), 5188, DOI: **10.1103/PhysRevB.13.5188**.
64 A. Togo, L. Chaput, T. Tadano and I. Tanaka, Implementation strategies in phonopy and phono3py, *J. Phys.: Condens. Matter*, 2023, **35**(35), 353001.
65 S. Nosé, A unified formulation of the constant temperature molecular dynamics methods, *J. Chem. Phys.*, 1984, **81**(1), 511–519.
66 W. G. Hoover, Canonical dynamics: equilibrium phase-space distributions, *Phys. Rev. A: At., Mol., Opt. Phys.*, 1985, **31**(3), 1695.
67 S. Ahmad, K. Sohail, L. Chen, H. Xu, H. Din and Z. Zhou, Type-II van der Waals heterostructures of GeC, ZnO and Al_2SO monolayers for promising optoelectronic and photocatalytic applications, *Int. J. Hydrogen Energy*, 2023, **48**(65), 25354–25365.
68 M. Demirtas, M. J. Varjovi, M. M. Çiçek and E. Durgun, Tuning structural and electronic properties of two-dimensional aluminum monochalcogenides: prediction of Janus Al_2XX' (X/X′: O, S, Se, Te) monolayers, *Phys. Rev. Mater.*, 2020, **4**(11), 114003.
69 T. Jungwirth, X. Marti, P. Wadley and J. Wunderlich, Antiferromagnetic spintronics, *Nat. Nanotechnol.*, 2016, **11**(3), 231–241.
70 I. Fina, X. Marti, D. Yi, J. Liu, J. Chu, C. Rayan-Serrao, S. Suresha, A. Shick, J. Železný, T. Jungwirth, *et al.*, Anisotropic magnetoresistance in an antiferromagnetic semiconductor, *Nat. Commun.*, 2014, **5**(1), 4671.
71 V. Baltz, A. Manchon, M. Tsoi, T. Moriyama, T. Ono and Y. Tserkovnyak, Antiferromagnetic spintronics, *Rev. Mod. Phys.*, 2018, **90**(1), 015005.
72 X. Li and X. Wu, Two-dimensional monolayer designs for spintronics applications, *Wiley Interdiscip. Rev.: Comput. Mol. Sci.*, 2016, **6**(4), 441–455.
73 X. Li and J. Yang, First-principles design of spintronics materials, *Natl. Sci. Rev.*, 2016, **3**(3), 365–381.